CORA Cork Open Research Archive
Cartlann Taighde Oscailte Chorcaí

Title	Core-shell tin oxide, indium oxide, and indium tin oxide nanoparticles on Si with tunable dispersion: Electrochemical and structural characteristics as a hybrid Li-ion battery anode
Authors	Osiak, Michal J.;Armstrong, Eileen;Kennedy, Tadhg;Sotomayor Torres, Clivia M.;Ryan, Kevin M.;O'Dwyer, Colm
Publication date	2013-08-16
Original Citation	Osiak, M. J., Armstrong, E., Kennedy, T., Sotomayor Torres, C. M., Ryan, K. M. and O'Dwyer, C. (2013) 'Core–Shell Tin Oxide, Indium Oxide, and Indium Tin Oxide Nanoparticles on Silicon with Tunable Dispersion: Electrochemical and Structural Characteristics as a Hybrid Li-Ion Battery Anode', ACS Applied Materials & Interfaces, 5(16), pp. 8195-8202. doi: 10.1021/am4023169
Type of publication	Article (peer-reviewed)
Link to publisher's version	https://pubs.acs.org/doi/pdf/10.1021/am4023169 - 10.1021/am4023169
Rights	© 2013 American Chemical Society. This document is the Accepted Manuscript version of a Published Work that appeared in final form in ACS Applied Materials & Interfaces, copyright © American Chemical Society after peer review and technical editing by the publisher. To access the final edited and published work see https://pubs.acs.org/doi/pdf/10.1021/am4023169
Download date	2026-11-16 05:58:47
Item downloaded from	https://hdl.handle.net/10468/6138

UCC
University College Cork, Ireland
Coláiste na hOllscoile Corcaigh

Core-shell tin oxide, indium oxide, and indium tin oxide nanoparticles on Si with tunable dispersion: Electrochemical and structural characteristics as a hybrid Li-ion battery anode

*Michal J. Osiak[1], Eileen Armstrong[1], Tadhg Kennedy[2,3], Clivia M. Sotomayor Torres[4,5,6], Kevin M. Ryan[2,3], and Colm O'Dwyer[1,3,7]**

[1] Department of Chemistry, University College Cork, Cork, Ireland

[2] Department of Chemical and Environmental Sciences, University of Limerick, Limerick, Ireland

[3] Materials & Surface Science Institute, University of Limerick, Limerick, Ireland

[4] Catalan Institute of Nanotechnology, Campus UAB, Edifici CM3, Bellaterra, 08193 (Barcelona) Spain

[5] Catalan Institute for Research and Advances Studies (ICREA), 08010 Barcelona, Spain

[6] Department of Physics, Universidad Autonoma de Barcelona, Campus UAB, 08193 Bellaterra, Spain

[7] Micro & Nanoelectronics Centre, Tyndall National Institute, Dyke Parade, Cork, Ireland

Keywords: Lithium Ion batteries, tin oxide, nanoparticles, anode, fundamental electrochemistry

Abstract

Tin oxide (SnO_2) is considered a very promising material as a high capacity Li-ion battery anode. Its adaption depends on a solid understanding of factors that affect electrochemical behavior and performance such as size and composition. We demonstrate here, that defined dispersions and structures can improve our understanding of Li-ion battery anode material architecture on alloying and co-intercalation processes of Lithium with Sn from SnO_2 on Si. Two different types of well-defined hierarchical Sn@SnO_2 core-shell nanoparticle dispersions were prepared by molecular beam epitaxy (MBE) on silicon, composed of either amorphous or polycrystalline SnO_2 shells. In_2O_3 and Sn doped In_2O_3 (ITO) NP dispersions are also demonstrated from MBE nanoparticle growth. Lithium alloying with the reduced form of the NPs and co-insertion into the silicon substrate showed reversible charge storage. Through correlation of electrochemical and structural characteristics of the anodes, we detail the link between the composition, areal and volumetric densities and the effect of electrochemical alloying of Lithium with Sn@SnO_2 and related nanoparticles on their structure and, importantly, their dispersion on the electrode. The dispersion also dictates the degree of co-insertion into the Si current collector, which can act as a buffer. The compositional and structural engineering of SnO_2 and related materials using highly defined MBE growth as model system allows a detailed examination of the influence of material dispersion or nanoarchitecture on the electrochemical performance of active electrodes and materials.

I. Introduction

Lithium-ion batteries are widely used today in portable electronics, telecommunication and medical devices. Li-ion technologies are rechargeable and offer advantages such as high energy density, lack of unwanted memory effects and relatively long cycle lifetimes [1-4]. Rapidly developing new technologies require lithium ion batteries with even higher capacities, better rate performance and increased safety for advanced applications and to satisfy consumer demand for portable electronic devices needing greater power over longer time periods [5, 6]. However, current battery anodes made from layered graphitic carbon are limited by a theoretical capacity of 372 mAh g^{-1} [7], which limits the overall cell capacity when paired with a high capacity cathode material. Additionally, higher rates tend to lower the overall cell capacity and voltage even for well-established Li-ion chemistries with defined discharge protocols, and so the ongoing search for high capacity, high-rate-capable, safe and stable materials and chemistries, continues.

Considerable research is therefore being directed to the study of emerging alternative anode materials with higher capacities such as Sn (990 mAh g^{-1}) [8], SnO (876 mAh g^{-1}), SnO_2 (780 mAh g^{-1}) [7, 9-14], Sb (660 mAh g^{-1}) [15], Si (4200 mAh g^{-1}) [16] and Ge (1600 mAh g^{-1}) [17]. Among these materials, SnO_2 is receiving renewed interest due to its simpler synthesis and reports of improving performance [7, 13, 18-20]. However, SnO_2 (like all the materials listed above) undergoes drastic volume changes (~200%) when electrochemically alloying with lithium after being reduced to metallic Sn during repeated charge/discharge cycles [21]. These changes may cause capacity loss and poor cycle life, which can come from loss of electrical contact between the active material and current collector as well from agglomeration of active material, preventing electrolyte access to the surface of the active material [22]. Preparing nanostructures with shorter diffusion lengths may greatly improve the rate capability of SnO_2 based anodes by allowing one dimension of the crystal structure to be smaller than the characteristic diffusion

length of Li^+ [23]. Additionally, the lower dimensionality would not negatively influence electronic conduction in most intercalation or alloying materials as the resistance of a 2D version of a 3D material would not greatly increase. Moreover, investigation of the density of active materials or their architecture in an electrode could lead to better understanding of their influence on all important aspects of a battery anode operation, including protective SEI layer formation.

Effective strategies have been proposed to resolve issues arising in SnO_2 based Li-ion battery anodes. Among them, synthesis of nanoscale SnO_2 with porous, layered, or multiphasic structures, such as nanoparticles [24], nanosheets [25, 26], nanotubes [26, 27] and core-shell nanostructures [28, 29] have been investigated. These reports demonstrated the sensitivity of performance to the nanoscale structure. These types of structures allow for a high density of materials with small diffusion lengths which improves Li^+ insertion rates [30]. High porosity is effective in allowing the stress caused by expansion and contraction to be accommodated so long as the electrochemical properties and electrical conductivity are not adversely affected. However, most of these structures are metastable and do not markedly improve long term cycle stability [31]. As an alternative, various composites have been proven to be more effective in enhancing the stability of SnO_2 based electrodes [32, 33]. Solvothermal and hydrothermal and microwave processes [34, 35], plasma jet reactor synthesis [36], AAO assisted etching [37] and various other templating methods [38-41] were extensively used to prepare nanorods, nanoplates, nanowires, and core-shell particles of SnO_2. A number of composite structures (such as CNT-SnO_2 or Fe_3O_4/SnO_2) [24, 42, 43] were also developed that demonstrated a large influence of their composite morphology and chemistry on the performance as an anode [44-47]. More investigation is needed to understand the changes occurring at the interface between the active materials and their interference with current collector, especially in the situation where the current collector can also react with lithium. Current collectors that can provide reversible charge storage

capabilities are not always beneficial and can adversely affect the interface to the active material. In cases where co-insertion (reversible) can be accommodated in such hybrid electrodes, there is potential for the provision of a degree of protection from volume change stress [48]; buffering Li^+ insertion can be very useful in cases where the expansion rates of the material are associated with excessive stress and strain, causing loss of electrical contact and mechanical integrity in porous or discontinuous active materials penetrated by electrolyte, and requires further investigation.

Compared to commonly used techniques, molecular beam epitaxy (MBE) offers excellent control over the crystalline quality, phase and morphologies of deposited structures, and their chemical composition. These benefits make MBE an ideal method for detailed investigations of electroactive materials with very well defined compositions, shapes and crystallinity [49].

In this paper, we demonstrate the growth of several novel types of $Sn@SnO_2$ core-shell nanoparticle dispersions prepared by MBE [50] on silicon, and through electron microscopy and spectroscopies, detail their respective behaviour in response to lithium alloying as Li-ion battery anodes. Oxidative crystallization in air after deposition of the respective metal (Sn, In, or both for ITO) results in a characteristic size dispersion of epitaxial SnO_2 nanoparticles with core-shell structure, and also In_2O_3 and Sn-doped In_2O_3 (ITO) nanoparticles. Detailed structural characterization and electrochemical cycling was carried out to elucidate how the reversible alloying process with Li is inherently dependent on size dispersion, core-shell structure and composition. The volumetric expansion of Si (that acts as the current collector) during lithium insertion is observed to provide a degree of mechanical buffering against loss of electrical contact between SnO_2 NPs. This work defines the influence of controlled crystal structure, architecture and volumetric/spatial density on the electrochemical processes occurring in a $Sn@SnO_2$-Si hybrid nanomaterial anode, and also the structural changes associated with Li

alloying and dealloying process introduced by cycling in a series of core-shell SnO_2 In_2O_3 and ITO NPs on silicon.

Experimental

Prior to the deposition, the surface of silicon was cleaned using standard RCA silicon cleaning procedures. After rinsing, a second treatment in a H_2O_2:HCl:H_2O (1:1:5) solution was used to remove metallic and organic contamination. For deposition of Sn and In, a custom-built MBE high-vacuum chamber with two high temperature effusion cells for metallic Sn or In targets, combined with an electron beam evaporator was designed in cooperation with MBE Komponenten GmbH. A uniform layer of Sn metal was deposited at pre-defined rates on a Si(100) substrate at a predefined temperature , with precise control over the nominal thickness (see Supporting Information Section S1 for the details of deposition process, thickness control and calibration). Similar procedure was followed for the deposition of In to form In_2O_3 nanoparticles. For formation of ITO, Sn and In were used at 10:90 weight ratio.

Surface morphologies and the chemical composition of the nanostructured dispersions were investigated by scanning electron microscopy (SEM) using a Hitachi SU-70 with an Oxford-50mm^2 X-Max detector for energy dispersive X-ray analysis (EDX). The acceleration voltage used for imaging was equal to 10 kV, unless stated otherwise. Transmission electron microscopy (TEM) analysis was conducted with a JEOL JEM-2100F field emission microscope operating at 200 kV, equipped with a Gatan Ultrascan CCD camera and EDAX Genesis EDS detector for atomic resolution crystal structure and composition examination. The size distribution of the nanodots was analyzed using ImageJ [51].

Cross-sectioning of the SnO_2 nanoparticles formed by MBE was carried out with an FEI Helios Nanolab Dual Beam FIB System. A protective layer of platinum was deposited over the surface of the sample to minimize surface damage. Cross-sectional TEM sample

preparation was performed on the slice using a standard FIB lift out technique described elsewhere [52].

X-ray photoelectron spectroscopy (XPS) was acquired using a Kratos Axis 165 monochromatized X-ray photoelectron spectrometer equipped with a dual anode (Mg/Al) source. Survey spectra were captured at as pass energy of 100 eV, step size of 1 eV, and dwell time of 50 ms. The core level spectra were an average of 10 scans captured at a PE of 25 eV, step size of 0.05 eV, and dwell time of 100 ms. The spectra were corrected for charge shift to the C 1s line at a binding energy of 284.9 eV. A Shirley background correction was employed, and the peaks were fitted to Voigt profiles.

To investigate the electrochemical insertion (alloying) and removal of Li, cyclic voltammetry measurements were carried out in a 3-electrode setup using a Multi Autolab 101 potentiostat, using Li as both counter and reference electrodes. All potentials, unless otherwise stated, are relative to Li^+/Li. Custom build Swagelok-type cells were used with counter and active material electrode separated by a polypropylene separator soaked in 1 mol dm^{-3} solution of $LiPF_6$ in ethylene carbonate:dimethyl carbonate (EC:DMC) in a 50:50 v/v ratio. The electrodes were potentiodynamically cycled using a scan rate of 0.2 mV s^{-1}. Afterwards, the electrodes were carefully washed in acetonitrile and a 10^{-4} mol dm^{-3} solution of acetic acid to remove the electrolyte residue.

II. Results and discussion

A. Core-shell Sn@SnO_2 nanoparticle dispersions

MBE growth of Sn at elevated temperatures (400°C-600°C) and subsequent oxidation in air results in the formation of two different types of SnO_2 core-shell nanoparticles (NPs) as shown in Fig 1a. The first type of NPs consists of highly crystalline Sn metal core NPs with a thin

amorphous coating of SnO_2 (ATO), and the second type comprises a crystalline Sn metal core with a polycrystalline SnO_2 shell (PCTO), forming Sn@SnO_2 NPs. Both are formed by simple two step deposition and oxidation mechanism. The SEM image in Fig. 1b shows a dispersion of ATO NPs on the Si substrate (optical images of the NP dispersions are shown in Supporting Information, Figure S2). ATO NPs typically have a high size dispersion, ranging from a few nm to over 500 nm in diameter, with an average interparticle distance of ~60 nm, covering about 65% of the sample surface (For detailed size dispersion analysis procedure see Supporting Information Section 2). The NPs are generally close to hemispherical shape, with some deviations probably related to their crystallization process. Small NPs are interspersed between the larger ones indicating that the growth undergoes simultaneous and progressive Sn deposition, surface diffusion of nucleated crystals and coalescence of neighboring particles.

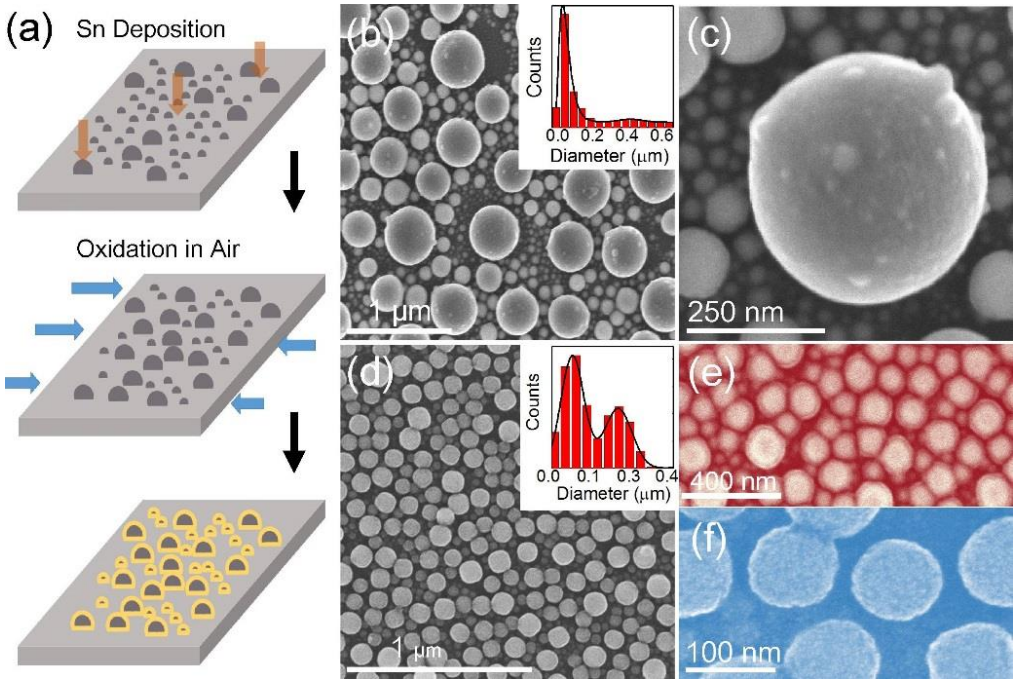


Figure 1. (a) Schematic diagram highlighting steps in formation of core-shell SnO_2 NPs. (b) SEM image showing the ATO NP dispersion. Inset shows the diameter distribution for ATO NPs. (c) High resolution SEM image showing a single ATO NP with small crystallites growing on the surface. (d) SEM image of PCTO NP layer. Inset: diameter distribution histogram for PCTO NP layer. (e) Low voltage (2 kV) SEM image of PCTO layer showing the core-shell structure of the NPs. (f) High resolution SEM image of PCTO NP layer showing texturing of the NP surface.

The high resolution SEM image in Fig. 1c shows that some of the larger ATO NPs also have smaller NPs growing on their surface. The smaller hierarchical NPs that form on the surface or larger NPs, is believed to occur when the coalescence mechanism that forms larger NPs is interrupted by oxidative crystallization of the liquid-phase Sn droplets on the larger NP surface. Defect-related or roughness-induced nucleation sites characteristic of some MBE growth likely contributes to the roughness development on the NPs. In_2O_3 NPs layers grown by MBE also showed similar hierarchical structure, with additional nanowire growth sometimes found from these crystallite seeds [48]. The exact origin of the nanocrystallites on the surface of the ATO NPs is however unclear. Crystalline core-polycrystalline shell NPs of SnO_2 (PCTO) are shown in Figs 1d-f, where their core-shell structure is visible in the low voltage secondary electron image in Fig. 1e. Analysis shows a much smaller size dispersion and lower average interparticle distance (~25 nm), which is related to lower deposition temperature, allowing particles to form without as much surface diffusion in their liquid state as found for ATO NPs. Compared to the ATO NPs, the PCTO NPs show much lower size dispersion, with the majority of the NPs ~100 nm in diameter (Fig. 1d inset) ;the total surface coverage is higher than for ATO NPs, amounting to ~80% coverage of the sample surface. High magnification SEM imaging of the NP shows a texture on the surface (Fig. 1f) which is associated with surface roughness (shown also in Fig. 2) specifically from the structure of the polycrystalline shell. During MBE, the small interfacial strain between the deposited film and the substrate greatly influences the structure growth. For low lattice mismatch, the growth will follow the Stranski-Krastanov (SK) mode [53], corresponding to complete wetting of the substrate surface by the deposited adatoms followed by formation of islands. Here, these islands are initially liquid, as the deposition is carried out above the melting temperature of Sn. Surface diffusion of liquid droplets occurs in parallel with the deposition, leading to coalescence of nearest-neighbour particles and formation of SnO_2 NPs upon subsequent oxidative crystallization in

ambient air. The smaller NPs interspersed between larger crystals cover a large portion of the substrate (~30%), indicating that progressive deposition of Sn resulted in formation of large number of small nanodroplets which then coalesced through surface diffusion to form large crystals. The coalescence occurs at slower rate (lower substrate temperature) in case of PCTO NPs resulting in better monodispersity in the surface coverage.

The amorphous layer formed around the crystalline core in ATO NPs is shown in Figs 2a and b. Both amorphous and polycrystalline shells (shown in Figs 2c and d), are formed during oxidative crystallization of the outer layer of the Sn droplet after the deposition. TEM analysis confirms that some of the small crystallites growing on the surface of large ATO particles also exhibit core-shell structure.

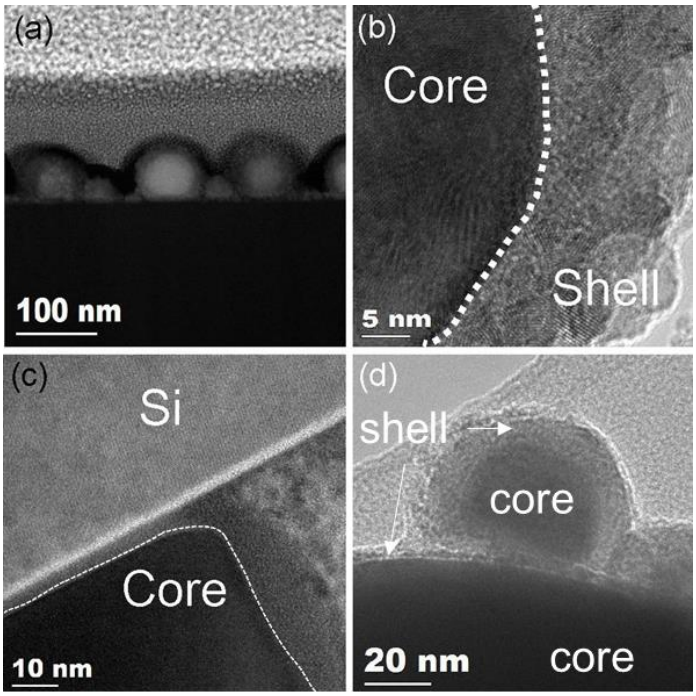


Figure 2. (a) Dark-Field TEM image showing a cross-section through a layer of PCTO NPs. (b) TEM image showing a cross-section of a single PCTO NP. (c) FIB cross-section through a single ATO NP, highlighting formation of amorphous shell beneath the contact point of NP with the substrate. (d) TEM image of NPs grown hierarchically on the surface of ATO NP.

This hierarchical consistency in core-shell construction indicates that formation of the surface crystallites and NP shells were simultaneous; the thickness of the ATO shell is similar for all particles, despite the 1-2 orders of magnitude difference in core diameter. Moreover, the structure of the crystallites on the surface of ATO is similar to the structure of the PCTO, with a polycrystalline shell around a crystalline core forming a hierarchy of core-shell NPs. The thickness of the amorphous layer is ~10 nm for all NPs on the surface of the substrate or those on other NPs, and the shell also extends below the contact point with the substrate (Fig. 2c) as well as at the interface between hierarchical core-shell NPs. This suggests that the formation of the amorphous shell progresses through diffusion of the oxygen through the top layer of the crystalline Sn. The thickness of polycrystalline shell in case of PCTO NPs is of similar order to the ATO NP shell (7-13 nm). This indicates a similar shell formation rate for both NPs.

To analyze chemical composition of the ATO and PCTO NPs XPS and EDX spectral measurements were carried out. The Sn 3d core level spectra for both ATO and PCTO samples are presented in Fig. 3a. The 3d core-level spectra from Sn in both PCTO and ATO NP structures contain a doublet with binding energies of 487 eV ($3d_{5/2}$) and 495.3 eV ($3d_{3/2}$) referenced to the C1s core level of 284.8 eV, (see Supporting Information Fig. S4) which suggests the (IV) oxidation state of Sn, *i.e.* SnO_2. A slight shift of 0.1 eV between PCTO and ATO core levels is equal to the measured shift in their respective adventitious C1s core levels.

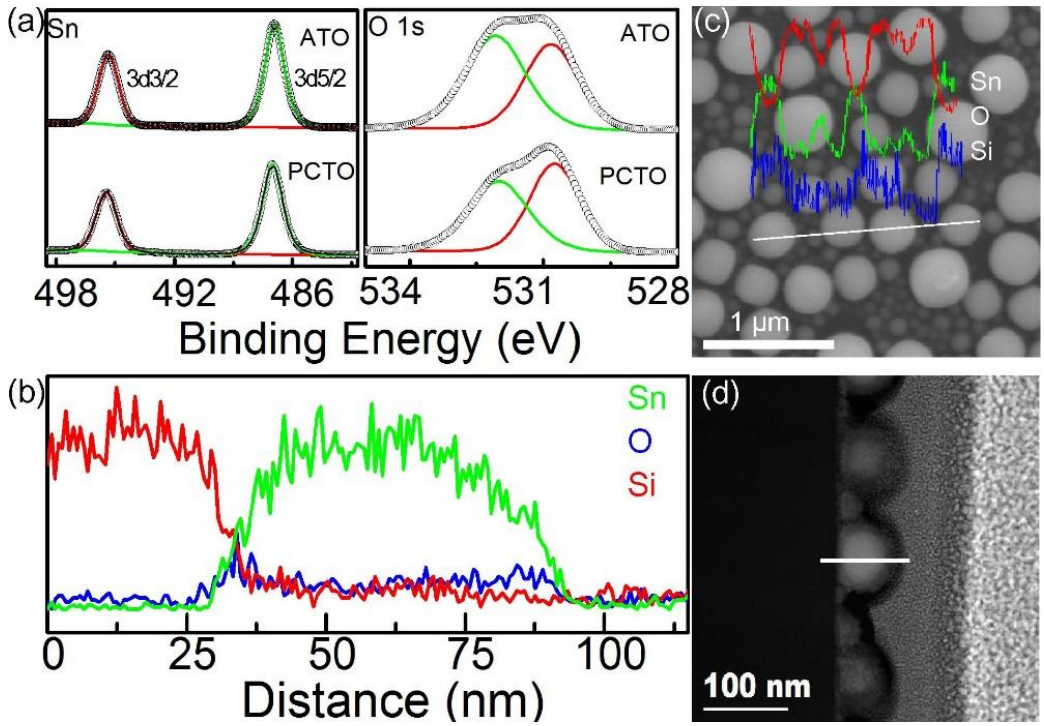


Figure 3. (a) Sn 3d and O1s core level spectra for ATO and PCTO NPs. (b) EDX linescan of the PCTO NP cross-section shown in (d). (c) EDX linescan of the surface of the ATO NPs. (d) Darkfield TEM image of PCTO NP layer. Line indicates the measurement site for the linescan presented in (b).

It is important to note that the differentiation between SnO and SnO_2 in photoemission studies is complicated due to only a very small shift in the Sn 3d core level binding energy. Consequently, stoichiometric ratios of elements were calculated from the XPS spectra according to [54]: $S_{ij} = \frac{C_i}{C_j} = \frac{I_i/ASF_i}{I_j/ASF_j}$ where C_i and C_j are the concentrations, I_i, I_j are the background corrected photoelectron emission line intensities, and ASF_i, ASF_j are the atomic sensitivity factors for photoionization of the *i*th and *j*th elements. Following this procedure we determined the concentration of oxygen (O) to be ~2 times the concentration of Sn, which corresponds to the SnO_2 stoichiometry of the oxide formed on the surface of the sample.

Furthermore, intensities for the deconvoluted O1s signals are not equal for both core-shell structures. This can be attributed to different silicon surface coverage of the sample with the NPs. In the case of ATO, the intensity of the deconvoluted O1s peak located at 532.1 eV,

related to oxygen in SiO_x is higher than for PCTO. As the surface coverage of the sample is larger for PCTO than ATO, it is expected that SiO_x signal would be higher for ATO NPs with lower surface coverage. The EDX line spectra taken from the FIB cross section of PCTO and the surface of ATO sample, also corroborate these results. Particularly, in Fig. 3b, an increase in measured intensity of the O Kα line indicates larger concentration of oxygen atoms close to the edges of the NP indicating the core shell of PCTO NPs. SEM EDX line-scan taken from the surface of the ATO NP layer also confirms oxygen presence within the penetration depth of the EDX beam, corroborating XPS results.

B. Reversible lithiation in core-shell SnO_2 NPs

As SnO_2 based materials are being considered for use as anodes for Li-ion secondary batteries[32, 55], its electrochemistry with lithium was investigated here for a variety of structures including core-shell SnO_2 NPs, but also comparative In_2O_3 and ITO NP dispersions and. There are limited reports on Si-Sn composites as Li-ion battery anodes [56], and so both ATO and PCTO NP alloying reactions with lithium, and the structural changes of the NPs and their dispersions on Si during lithiation processes were investigated with cyclic voltammetry and high resolution ex-situ electron microscopy. The Li alloying reaction with the Sn NP core is possible if the outer oxide coating can be reduced to Sn^0 from the respective SnO_2 on PCTO and ATO NPs.

Cyclic voltammetry was used to investigate this process. In a CV each alloying, growth, removal, oxidation and reduction process can be examined in each cycle, at the respective potential for each process. This is especially useful in the present case, where numerous processes and several materials are present. The cathodic processes involve the alloying of Li with the reduced form of SnO_2 to form a Li-Sn alloy (charging) and the anodic process follows Li extraction or dealloying (discharging). There is a substantial difference between CVs for ATO (Fig. 4a) and PCTO (Fig 4b). The large irreversible peak (indicated in the CVs by **I**) is

typically regarded as being due to the formation of a stable SEI layer and to electrochemical reduction of SnO_2 to a system of three phases consisting of LiO_2, O_2 and SnO. Mohamedi *et al.* detailed these reaction products and their formation when examining amorphous SnO_2 films prepared by electrostatic spray deposition at elevated temperature [57]. This reaction is complete at ~1.5 volts and is present in both CVs. Subsequently, SnO is reduced to metallic Sn, indicated by large peak present at ~1 V for both systems (**I** for PCTO, **II-III** for ATO). A shift in voltage for this peak occurs in subsequent cycles for PCTO, indicating improved kinetics of the reaction as well as decreased lithium concentration in the phase formed at that peak potential.. Two reversible peaks appear in the cathodic scan (**V–VI** for ATO, **V-VII** for PCTO) which can be attributed to the formation of particular Li alloys with Sn: $Li_{2.33}Sn$ formed at 0.55 V and $Li_{4.4}Sn$ is formed at 0.15 V. Oxidation peaks appearing at 0.57 V, 0.81 V, 0.87 V, 0.91 V and 1.21 V correspond to the dealloying of Li_xSn and partially reversible oxidation of Sn to SnO_2. The full electrochemical process occurring during reversible alloying of lithium with Sn can be described[58] by the following set of equations:

$$Li^+ + e^- + electrolyte \rightarrow SEI \qquad (1)$$

$$SnO_2 + 4\,Li^+ + 4e^- \rightarrow Sn + 2\,Li_2O \quad (2)$$

$$Sn + xLi^+ + xe^- \leftrightarrow Li_xSn\ (0 < x < 4.4) \quad (3)$$

The reaction in Eqn. 2 is normally regarded as irreversible and a cause of capacity loss in Sn-based anodes regardless of consistency in electrical connectivity of the active material, phase conversion, and resistance changes, while in this case the reduction peak at 1.25 V (**I** for ATO and PCTO NPs) and corresponding oxidation peak at 1.23 V (**VI** for ATO NPs, **VII** for PCTO NPs) remain stable over the 5 cycles indicating partial reversibility of this reaction compared to bulk SnO_2. Moreover, a small amount of lithium is introduced into the silicon current collector. The insertion and removal potentials for silicon are typically 0.2 V and 0.5

V, respectively (dedicated CVs for Si(100) electrodes without NPs are shown in Supporting Information Fig. S5). The relatively higher rate of reaction as shown by the larger current in this potential range indicates insertion of lithium into Si coexists with alloying of lithium with Sn.

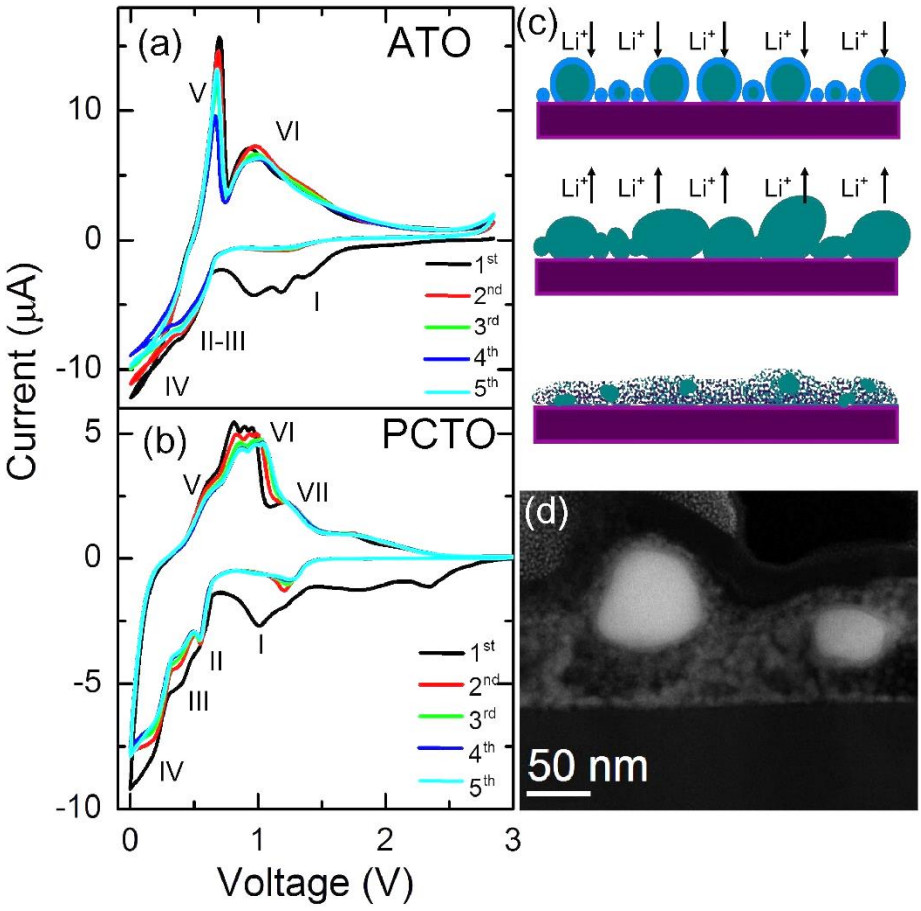


Figure 4. (a) Cyclic voltammograms for ATO and (b) PCTO NPs on silicon. (c) Schematic diagram describing formation of porous NP layers upon lithiation cycling. (d) Dark-field STEM image showing highly porous layer comprising pulverized NPs formed by electrochemical cycling of the PCTO NP layer. The brighter regions are Sn and SnO_2.

For ATO NPs, the large irreversible area in the 1.6-0.8 V range (**I**), corresponds to reduction of SnO_2 to metallic Sn, and the succeeding peak at 0.39 V (**II-III**) corresponds to formation of a Li_xSn phase, where x ranges from $0 < x < 4.4$. This is also found for the PCTO NPs, implying that the crystal structure of the thin shell coatings are less critical than their

stoichiometric phases, which are identical. In the lower voltage range corresponding to insertion of lithium into Si, a large peak at ~0.1 V (**IV**) is present. In the anodic part of the CV, two reversible peaks at ~0.65 V (**V**) and ~1 V (**IV**) are found. The first peak can be attributed to the removal of lithium from silicon while the second corresponds to removal of lithium from Sn[23], and it occurs at a similar voltage in both ATO and PCTO core-shell NPs.

The Si insertion and removal rates as indicated by the current in corresponding CV peaks increase with cycling, indicating an activation effect characteristic for Si-based anodes[2, 16, 59-61]. Specifically, volumetric expansion of lithiated material causes cracks and exposure of unreacted Si to the electrolyte, which in turn allows more lithium to be incorporated into material at the same potential. Usually it is considered a negative effect, causing an increasing degree of cracking and loss of electrical contact between the active material and the current collector. As it is not the active material, expansion occurs only where the SnO_2 NPs are not present. Comparing the differences between the ATO and PCTO NPs and their spatial density and size dispersion on the Si, ~25% higher rate of lithium insertion into ATO sample is observed, which correlates well with the surface coverage difference between ATO and PCTO. Moreover, formation of an SEI layer (from the voltammetric response) is more pronounced for PCTO samples, which can be attributed to a higher areal mass loading of polycrystalline SnO_2 shell.

To further analyze changes induced in the structure of the anode during lithiation, FIB cross-sections of both types of NPs were investigated by TEM (Fig. 5). Figure 5a shows an SEM image of the ATO NP layer after cycling. A change in ATO NP shape is found (see Fig. 1b and Fig. 5a inset for comparison), but significantly, the size of the ATO NP has not increased laterally. PCTO NPs on the other hand, shows extensive modification after cycling (shown in Fig. 5b). The NP underwent pulverization likely due to expansion and contraction during cycling that results in a higher density of smaller NPs on the surface. The initial interparticle

distances between ATO NPs are significantly larger than between PCTO NPs and are devoid of NP-NP contacting within the layer. PCTO NPs are, prior to lithiation, formed with much smaller interparticle distances, and thus the expansion during lithium insertion will lead to larger degree of NP agglomeration and coalescence.

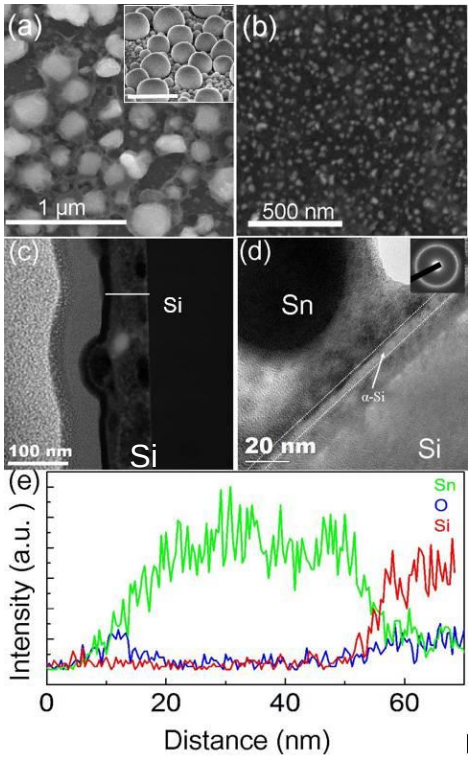


Figure 5. (a) SEM images showing a layer of ATO NPs before (inset, scalebar 500 nm) and after cycling. (b) SEM image showing PCTO NP layer after cycling. (c) Dark-field TEM image showing a porous layer formed due to electrochemical cycling of PCTO NPs. White line indicates the site for the line-scan presented in (e). (d) TEM image showing the interface between the silicon current collector and the PCTO NP layer after cycling, with α-Si layer highlighted. (e) EDX line-scan through PCTO NP layer after cycling. Site of measurement is indicated by the white line in (c).

Figure 5c shows a dark-field TEM cross-section of the PCTO NP layer. The structural changes confirm the observation from Fig. 5b, (see Fig. 2 for comparison) where the NP layer is transformed into a porous layer of Sn nanocrystals after cycling that are much smaller (by a factor of ~4) than their as-formed size. Bright areas (larger atomic weight electron scatterers) seen in Fig. 5c correspond to Sn present in the resulting layer. The existence of a porous layer with thickness corresponding to the diameter of the largest PCTO

indicates that the expansion of NPs allows for agglomeration and coalescence of nearest neighboring NPs during charge-discharge cycles. Multiple NP expansions can cause the formation of a largely porous, but also highly interconnected layer. A small number of the NPs are still present in their metallic non-distorted form (see Fig. 5d and the white particle in Fig. 5c) probably due to lack of contact with the electrolyte after initial phase of the reaction.

The stability of the contact is in this case is mainly caused by co-insertion of the lithium into silicon current collector, which offers some degree of buffering by intercalating lithium ions at the Si-electrolyte interface that exceed the alloying limit of the volumetric density of NPs on the surface. As discussed further on, the lower areal density of SnO_2 NPs is correlated with a higher Si interface, and the Si interface allows some degree of buffering by intercalating excess Li^+ at lower potential to the alloying reaction with Sn. Such buffering effects have been observed in SnO_2/C composites, where the composite alleviates large scale material breakdown[62]. NPs were deposited on single crystalline Si, and the formation of α-Si layer underneath the porous PCTO (Fig. 5d, and further detail in Supporting Information, Fig. S5) layer after cycling indicates that the reversible Li_xSi Zintl phases[63, 64] of silicide are formed in parallel with expansion/contraction due to oxide reduction to metallic Sn and subsequent lithiation of the original PCTO NP. EDX analysis (Fig. 5e) also shows uniform distribution of Sn within the composite material matrix, confirming formation of a porous Sn layer. ATO NPs after 5 insertion-removal cycles seen in Figure 5a also show significant structural changes, mainly seen for the largest NPs. The elemental distribution post cycling is shown in Fig. 5e, confirming that the porous film consists of from Sn with Si interspersed in the layer close to the surface of the current collector.

The electrochemical response of NP dispersions was also examined for a range of NPs prepared by MBE: in addition to core-shell SnO_2, we investigated In_2O_3 and ITO NP dispersions whose CVs and corresponding size dispersions are presented in Fig. 6.

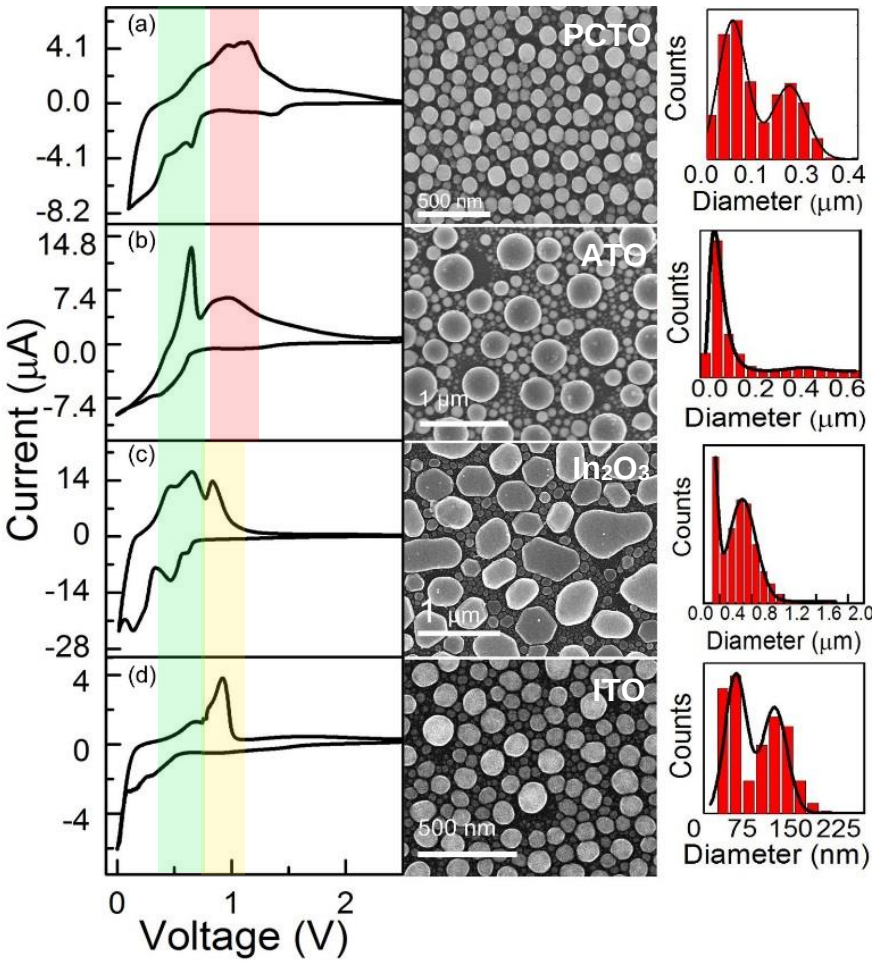


Figure 6. Single cycle voltammograms, SEM image of the surface of the NP layer, and corresponding size dispersion histogram for (a) PCTO NPs, (b) ATO NPs, (c) In_2O_3 NPs, and (d) Sn-doped In_2O_3 (ITO) NPs. De-intercalation potential windows are shaded for Li_xSi (green), Li_xSn (pink) and Li_xIn (yellow).

The cyclic voltammetric response of the various SnO_2 and In_2O_3 NPs dispersions in Fig. 6, show that the lithium insertion and removal characteristics are strongly dependent on the shape and size dispersion of the NPs and their volumetric density; all sample exhibit at least bimodal sizes, with one mode dominating in the case of highly coalesced ATO and In_2O_3 NP dispersions. As all are deposited from In, Sn or In + Sn using MBE, the distributions are characteristics of a similar formation mechanism, outlined earlier for SnO_2. In terms of electrochemical reduction, alloying, intercalation and the reverse processes, there is similarity

between responses for PCTO and ITO NPs (Figs 6a and d), and between ATO NPs and In_2O_3 NP layers (Fig. 6b and c).

Analysis of the data in Fig. 6 shows that both areal density and volumetric density need to be considered, especially when using hybrid systems such as the present case where the current collector (silicon) is capable of intercalating lithium. Lithium insertion and removal peaks for Li_xSi are more pronounced (as measured from the magnitude of the current and integrated charge) for ATO and In_2O_3 NP dispersions, while alloying reactions with active material (In, Sn) dominates for PCTO and ITO NP layers. This trend is due to the areal coverage, whereas the relative contribution of the alloying to intercalation response in these electrodes is linked to the volumetric density of active material. The shape of the voltammetric response in each case thus includes different relative contributions from the CV response of Li-Si formation (see Supporting Information Fig. S6). For the PCTO and ITO NP dispersions (Figs 6a and d), the Li_xSi phases (*cf.* Fig. 5) are observed, but dominated by the In- and Sn-containing material. As the volumetric density is lower for these electrodes (in spite of higher areal coverage), the corresponding currents are lower. The opposite trend is found for ATO and In_2O_3 NP dispersion with lower areal coverage, regardless of the volumetric density of active material.

In such cases, charging and discharging in specific potential windows can select the alloying and/or intercalation process where dissimilar materials are electrochemically active, but this work shows that the relative contributions are linked to the dispersion of the material in addition to its structure and composition. For much smaller PCTO and ITO NPs < 200 nm in diameter, all of the Li-Sn alloying occurs prior to co-insertion with silicon. During cycling however, material break is observed for SnO_2 when large (>250 nm) NPs are used. Generally, the dispersion of nanoscale active materials should also consider the diameter or thickness of the active material in addition to the effective porosity, especially in composite systems where

insertion or alloying occurs at different potentials via different mechanisms. By varying the dispersion and thus the effective porosity of the active material, hybrid electrodes involving electrochemically active current collectors can also offer some degree of stress-change buffering during deep charging and discharging.

III. Conclusions

Using molecular beam epitaxy, we detailed the growth of two distinct and well defined types of Sn/SnO_2 core-shell nanoparticles with crystalline metallic Sn cores and either amorphous or polycrystalline SnO_2 shells. In_2O_3 and Sn doped In_2O_3 (ITO) NP dispersions are also demonstrated using this approach. Electron microscopy and spectroscopy analyses confirmed a hierarchical core-shell structure of the SnO_2 NPs with different diameters to give a range of volumetric and areal densities of material. Lithium alloying with the reduced form of the NPs and co-insertion into the substrate (which also serves as current collector) showed reversible charge storage via alloying with Sn or In. The effect of lithium insertion and removal on different NP dispersions monitored by electron microscopy and cyclic voltammetry, showed that the electrochemical behavior depends on the relative size via the volumetric density of the NPs and their areal dispersion on the surface, in addition to their composition. The knowledge can be extended to a range of other active (nano)materials and systems so that active material arrangements and densities can influence performance, in addition to the structure, size and composition. In cases where the material spacing is larger the volumetric expansion can be accommodated radially while maintaining mechanical and electrical contact. In this regard, co-insertion into the Si facilitates this process and is dictated by the active material dispersion. The compositional and structural engineering on SnO_2 and related materials using highly

defined MBE growth as model system has allowed a detailed examination of the influence of material dispersion or nanoarchitecture on the electrochemical performance.

ASSOCIATED CONTENT

Supporting Information

Details of the deposition process, optical and SEM images, and size dispersion analysis are provided. This material is available free of charge via the Internet at http://pubs.acs.org.

AUTHOR INFORMATION

*To whom correspondence should be addressed: Fax: +353 21 427 4097; Tel: +353 21 490 2732; E-mail: c.odwyer@ucc.ie.

Author Contributions

The manuscript was written through contributions of all authors. All authors have given approval to the final version of the manuscript.

Acknowledgements

MO and EA acknowledge the support of the Irish Research Council under awards RS/2010/2170 and RS/2010/2920. The authors thank Dr Fathima Laffir for assistance in XPS measurements, and Prof. J. D. Holmes for access to the Electron Microscopy Analytical Facility at Tyndall National Institute. COD acknowledges support from Science Foundation Ireland under award no. 07/SK/B1232a, the UCC Strategic Research Fund, and from the Irish Research Council New Foundations Award.

References

1. Bruce, P. G.; Scrosati, B.; Tarascon, J.-M., *Angew. Chem. Int. Edit.* **2008,** *47* (16), 2930-2946.
2. Guo, Y. G.; Hu, J. S.; Wan, L. J., *Adv. Mater.* **2008,** *20* (15), 2878-2887.
3. Li, H.; Wang, Z. X.; Chen, L. Q.; Huang, X. J., *Adv. Mater.* **2009,** *21* (45), 4593-4607.
4. Ji, L. W.; Lin, Z.; Alcoutlabi, M.; Zhang, X. W., *Energ. Environ. Sci.* **2011,** *4* (8), 2682-2699.
5. Goodenough, J. B.; Kim, Y., *J. Pow. Sources* **2011,** *196* (16), 6688-6694.
6. Goodenough, J. B.; Kim, Y., *Chem. Mater.* **2009,** *22* (3), 587-603.
7. Chen, J. S.; Lou, X. W., *Small* **2013,** *9*, 1877-1893.
8. Winter, M.; Besenhard, J. O., *Electrochim. Acta* **1999,** *45* (1–2), 31-50.
9. Sivashanmugam, A.; Kumar, T. P.; Renganathan, N. G.; Gopukumar, S.; Wohlfahrt-Mehrens, M.; Garche, J., *J. Pow. Sources* **2005,** *144* (1), 197-203.
10. Li, N. C.; Martin, C. R.; Scrosati, B., *Electrochem. Solid St.* **2000,** *3* (7), 316-318.
11. Park, M. S.; Kang, Y. M.; Wang, G. X.; Dou, S. X.; Liu, H. K., *Adv. Funct. Mater.* **2008,** *18* (3), 455-461.
12. Zhou, G.; Wang, D. W.; Li, L.; Li, N.; Li, F.; Cheng, H. M., *Nanoscale* **2013,** *5* (4), 1576-82.
13. Chen, J. S.; Lou, X. W., *Mater. Today* **2012,** *15* (6), 246-254.
14. Chen, M. H.; Huang, Z. C.; Wu, G. T.; Zhu, G. M.; You, J. K.; Lin, Z. G., *Mater. Res. Bull.* **2003,** *38* (5), 831-836.
15. Aldon, L.; Garcia, A.; Olivier-Fourcade, J.; Jumas, J.-C.; Fernández-Madrigal, F. J.; Lavela, P.; Vicente, C. P.; Tirado, J. L., *J. Pow. Sources* **2003,** *119–121*, 585-590.
16. Kasavajjula, U.; Wang, C.; Appleby, A. J., *J. Pow. Sources* **2007,** *163* (2), 1003-1039.
17. Chockla, A. M.; Klavetter, K. C.; Mullins, C. B.; Korgel, B. A., *ACS Appl. Mater. Interfaces* **2012,** *4* (9), 4658-4664.
18. Wan, B.; Luo, B.; Xianlong, L.; Zhi, L., *Mater. Today* **2012,** *15* (12), 544-552.
19. Wang, C.; Zhou, Y.; Ge, M.; Xu, X.; Zhang, Z.; Jiang, J. Z., *J. Am. Chem. Soc.* **2009,** *132* (1), 46-47.
20. Chen, Y.; Ma, J.; Li, Q.; Wang, T., *Nanoscale* **2013,** *5* (8), 3262-3265.
21. Huggins, R. A., *Solid State Ion.* **1983,** *113-115*, 57-67.
22. Li, H.; Wang, Q.; Shi, L.; Chen, L.; Huang, X., *Chem. Mater.* **2001,** *14* (1), 103-108.
23. Park, M.-S.; Wang, G.-X.; Kang, Y.-M.; Wexler, D.; Dou, S.-X.; Liu, H.-K., *Angew. Chem. Int. Edit.* **2007,** *46* (5), 750-753.
24. Chen, J. S.; Cheah, Y. L.; Chen, Y. T.; Jayaprakash, N.; Madhavi, S.; Yang, Y. H.; Lou, X. W., *J. Phys. Chem. C* **2009,** *113* (47), 20504-20508.
25. Ohgi, H.; Maeda, T.; Hosono, E.; Fujihara, S.; Imai, H., *Cryst. Growth Des.* **2005,** *5* (3), 1079-1083.
26. Masuda, Y.; Kato, K., *J. Cryst. Growth* **2009,** *311* (3), 593-596.
27. Du, N.; Zhang, H.; Chen, B.; Ma, X.; Yang, D., *Chem. Commun* **2008,** (26), 3028-3030.
28. Lou, X. W.; Yuan, C.; Archer, L. A., *Small* **2007,** *3* (2), 261-265.
29. Yang, H. X.; Qian, J. F.; Chen, Z. X.; Ai, X. P.; Cao, Y. L., *J. Phys. Chem. C* **2007,** *111* (38), 14067-14071.
30. O'Dwyer, C.; Lavayen, V.; Tanner, D. A.; Newcomb, S. B.; Benavente, E.; Gonzalez, G.; Benavente, E.; Torres, C. M. S., *Adv. Funct. Mater.* **2009,** *19*, 1736-1745
31. Wang, F.; Yao, G.; Xu, M.; Zhao, M.; Sun, Z.; Song, X., *J Alloy Compd* **2011,** *509* (20), 5969-5973.
32. Courtney, I. A.; Dahn, J. R., *J Electrochem Soc* **1997,** *144* (6), 2045-2052.
33. Fan, J.; Wang, T.; Yu, C. Z.; Tu, B.; Jiang, Z. Y.; Zhao, D. Y., *Adv. Mater.* **2004,** *16* (16), 1432-1436.
34. Chen, Y. J.; Xue, X. Y.; Wang, Y. G.; Wang, T. H., *Appl.Phys. Lett.* **2005,** *87* (23), 233503.
35. Subramanian, V.; Burke, W. W.; Zhu, H.; Wei, B., *J. Phys. Chem. C* **2008,** *112*, 4550-4556.

36. Kumar, V.; Kim, J. H.; Pendyala, C.; Chernomordik, B.; Sunkara, M. K., *J. Phys. Chem. C* **2008,** *112* (46), 17750-17754.
37. Cheng, F.; Tao, Z.; Liang, J.; Chen, J., *Chem. Mater.* **2007,** *20* (3), 667-681.
38. Lou, X. W.; Wang, Y.; Yuan, C.; Lee, J. Y.; Archer, L. A., *Adv. Mater.* **2006,** *18* (17), 2325-2329.
39. Wang, Z.; Zhou, L.; Lou, X. W., *Adv. Mater.* **2012,** *24* (14), 1903-1911.
40. Ding, S.; Chen, J. S.; Qi, G.; Duan, X.; Wang, Z.; Giannelis, E. P.; Archer, L. A.; Lou, X. W., *J. Am. Chem. Soc.* **2010,** *133* (1), 21-23.
41. Chen, J. S.; Li, C. M.; Zhou, W. W.; Yan, Q. Y.; Archer, L. A.; Lou, X. W., *Nanoscale* **2009,** *1* (2), 280-285.
42. Chen, Y.-J.; Gao, P.; Wang, R.-X.; Zhu, C.-L.; Wang, L.-J.; Cao, M.-S.; Jin, H.-B., *J. Phys. Chem. C* **2009,** *113* (23), 10061-10064.
43. Lou, X. W.; Chen, J. S.; Chen, P.; Archer, L. A., *Chem. Mater.* **2009,** *21* (13), 2868-2874.
44. Liu, J.; Li, W.; Manthiram, A., *Chem. Commun* **2010,** *46* (9), 1437-1439.
45. Wen, Z.; Wang, Q.; Zhang, Q.; Li, J., *Adv. Funct. Mater.* **2007,** *17* (15), 2772-2778.
46. Cui, G.; Hu, Y.-S.; Zhi, L.; Wu, D.; Lieberwirth, I.; Maier, J.; Müllen, K., *Small* **2007,** *3* (12), 2066-2069.
47. Park, M.-S.; Kang, Y.-M.; Dou, S.-X.; Liu, H.-K., *J. Phys. Chem. C* **2008,** *112* (30), 11286-11289.
48. Osiak, M.; Khunsin, W.; Armstrong, E.; Kennedy, T.; Torres, C. M. S.; Ryan, K. M.; O'Dwyer, C., *Nanotechnology* **2013,** *24* (6), 065401.
49. Kim, D.-W.; Hwang, I.-S.; Kwon, S. J.; Kang, H.-Y.; Park, K.-S.; Choi, Y.-J.; Choi, K.-J.; Park, J.-G., *Nano Lett.* **2007,** *7* (10), 3041-3045.
50. O'Dwyer, C.; Szachowicz, M.; Visimberga, G.; Lavayen, V.; Newcomb, S. B.; Torres, C. M. S., *Nature Nanotech.* **2009,** *4*, 239-244.
51. Schneider, C. A., Rasband, Wayne S, Eliceiri, Kevin W, *Nat. Methods* **2012,** *9* (7), 671-675.
52. Giannuzzi, L. A.; Stevie, F. A., *Micron* **1999,** *30* (3), 197-204.
53. Chambers, S. A., *Surf. Sci. Rep.* **2000,** *39* (5–6), 105-180.
54. Ratner, B. D.; Castner, D. G., *Electron Spectroscopy for Chemical Analysis*. John Wiley & Sons, Ltd: Chichester, UK, 2009; p 47-112.
55. Inoue, H.; Mizutani, S.; Ishihara, H.; Hatake, S., *Meeting Abstracts* **2008,** *MA2008-02* (12), 1160-1160.
56. Yan-hong, L.; Yua, L.; Qiu, X.-p., *Chin. J. Proc. Eng.* **2011,** *11* (5), 870-874.
57. Mohamedi, M.; Lee, S.-J.; Takahashi, D.; Nishizawa, M.; Itoh, T.; Uchida, I., *Electrochim. Acta* **2001,** *46* (8), 1161-1168.
58. Zhao, Y.; Li, J.; Ding, Y.; Guan, L., *RSC Adv.* **2011,** *1* (5), 852-856.
59. Chan, C. K.; Peng, H.; Liu, G.; McIlwrath, K.; Zhang, X. F.; Huggins, R. A.; Cui, Y., *Nat. Nanotechnol.* **2008,** *3* (1), 31-35.
60. Li, H.; Huang, X. J.; Chen, L. Q.; Wu, Z. G.; Liang, Y., *Electrochem. Solid St.* **1999,** *2* (11), 547-549.
61. Obrovac, M. N.; Christensen, L., *Electrochem. Solid St.* **2004,** *7* (5), A93-A96.
62. Zhang, W.-M.; Hu, J.-S.; Guo, Y.-G.; Zheng, S.-F.; Zhong, L.-S.; Song, W.-G.; Wan, L.-J., *Adv. Mater.* **2008,** *20* (6), 1160-1165.
63. Wang, J. W.; He, Y.; Fan, F.; Liu, X. H.; Xia, S.; Liu, Y.; Harris, C. T.; Li, H.; Huang, J. Y.; Mao, S. X.; Zhu, T., *Nano Lett* **2013,** *13* (2), 709-15.
64. Green, M.; Fielder, E.; Scrosati, B.; Wachtler, M.; Moreno, J. S., *Electrochem. Solid St.* **2003,** *6* (5), A75-A79.

Table of Contents Graphic

